

Three-dimensional superresolution colocalization of intracellular protein superstructures and the cell surface in live *Caulobacter crescentus*

Matthew D. Lew^{a,b,1}, Steven F. Lee^{b,1,2}, Jerod L. Ptacin^c, Marissa K. Lee^b, Robert J. Twieg^d, Lucy Shapiro^c, and W. E. Moerner^{b,3}

^aDepartment of Electrical Engineering, Stanford University, Stanford, CA 94305; ^bDepartment of Chemistry, Stanford University, Stanford, CA 94305; ^cDepartment of Developmental Biology, Stanford University School of Medicine, Beckman Center, Stanford, CA 94305; and ^dDepartment of Chemistry, Kent State University, Kent, OH 44242

Contributed by W. E. Moerner, September 5, 2011 (sent for review July 25, 2011)

Recently, single-molecule imaging and photocontrol have enabled superresolution optical microscopy of cellular structures beyond Abbe's diffraction limit, extending the frontier of noninvasive imaging of structures within living cells. However, live-cell superresolution imaging has been challenged by the need to image three-dimensional (3D) structures relative to their biological context, such as the cellular membrane. We have developed a technique, termed superresolution by power-dependent active intermittency and points accumulation for imaging in nanoscale topography (SPRAIPAIN) that combines imaging of intracellular enhanced YFP (eYFP) fusions (SPRAI) with stochastic localization of the cell surface (PAINT) to image two different fluorophores sequentially with only one laser. Simple light-induced blinking of eYFP and collisional flux onto the cell surface by Nile red are used to achieve single-molecule localizations, without any antibody labeling, cell membrane permeabilization, or thiol-oxygen scavenger systems required. Here we demonstrate live-cell 3D superresolution imaging of Crescentin-eYFP, a cytoskeletal fluorescent protein fusion, colocalized with the surface of the bacterium *Caulobacter crescentus* using a double-helix point spread function microscope. Three-dimensional colocalization of intracellular protein structures and the cell surface with superresolution optical microscopy opens the door for the analysis of protein interactions in living cells with excellent precision (20–40 nm in 3D) over a large field of view (12 × 12 μm).

cell biology | wide-field microscopy | cytoskeleton | fluorescence microscopy | bacteria

Fluorescence microscopy and its associated labeling techniques have become invaluable tools for cell biologists because of their remarkable label specificity, high signal-to-background, and noninvasive nature. However, far-field conventional optical microscopy is limited by the diffraction limit to a lateral (xy) resolution of approximately $\lambda/2$ and an axial (z) resolution of approximately λ due to the finite numerical aperture of microscope objective lenses and diffraction of light of wavelength λ . X-ray (1) and electron (2) microscopes can provide higher spatial resolution but usually sacrifice contrast or specificity, involve more complex sample preparation, and are extremely difficult to use for live-cell imaging.

Recently, many superresolution optical microscopy methods have been developed to push fluorescence optical imaging beyond the diffraction limit in all three dimensions. One class, based on spatial patterning of the excitation and/or a nonlinear response, includes three-dimensional (3D) structured illumination microscopy (3), which improves resolution by a factor of two, and 3D stimulated emission depletion microscopy (4), which has been demonstrated to have an isotropic resolution of approximately 40 nm depending upon the emitter. The complementary class, denoted by the mechanism-independent term single-molecule active control microscopy (SMACM), includes

(fluorescence) photoactivated localization microscopy [(F) PALM] (5, 6), [direct (7)] stochastic optical reconstruction microscopy (STORM) (8), points accumulation for imaging in nanoscale topography (PAINT) (9, 10), photoswitching of fluorescent proteins (11), ground state depletion microscopy followed by individual molecule return (12), and blink microscopy (13). All of these pointillist techniques localize sparse subsets of single-molecule emitters sequentially over time, thereby building up a superresolution reconstruction, until the desired structure is resolved. Each of the aforementioned acronyms refers to the specific active control mechanism that is used to prevent single-molecule overlap in any one image by keeping the emitting concentration low, such as photoactivation, photoswitching, collisional flux from the surrounding solution, and pumping into reversible long-lived dark states.

Three-dimensional localizations are possible with SMACM techniques by breaking the axial symmetry of the standard point spread function (PSF) (14–16), imaging in multiple focal planes simultaneously (17), or projecting the axial dimension onto a lateral dimension (18). These methods can achieve precisions below 100 nm in 3D over a 2-μm range (14, 19, 20). In addition, sub-10-nm precision can be obtained via interferometry (21); however, these methods severely restrict the sample geometry, have a shallower operational depth of field (~650 nm) (22), and are not yet conducive to live-cell imaging.

Superresolution microscopy has been particularly useful in protein localization studies within bacterial cells (23) because of the comparable size of most bacteria relative to the visible diffraction limit. For example, *Caulobacter crescentus* is a bacterium whose physical dimensions (~2 × 0.6 μm) lie close to the resolving power of conventional optical microscopy (~250 nm). *C. crescentus* exhibits differential polar localization of regulatory proteins and polar organelles such as flagella and pili. Enhanced YFP (eYFP) has been used in superresolution imaging to observe multiple structures in *C. crescentus* including: a banded structure and a midplane ring formed by the protein MreB (11), eukaryotic spindle-like DNA segregation structure composed of the ATPase ParA (24), and the spatial distribution of the nucleoid-associated protein HU during different phases of the *C. crescentus* cell cycle (25). Although actual biological interactions occur in 3D space,

Author contributions: M.D.L., S.F.L., and W.E.M. designed research; M.D.L., S.F.L., and M.K.L. performed research; J.L.P., R.J.T., and L.S. contributed new reagents/analytic tools; M.D.L. and S.F.L. analyzed data; and M.D.L., S.F.L., J.L.P., L.S., and W.E.M. wrote the paper.

The authors declare no conflict of interest.

¹M.D.L. and S.F.L. contributed equally to this work.

²Present address: Department of Chemistry, University of Cambridge, Cambridge CB2 1EW, United Kingdom.

³To whom correspondence should be addressed. E-mail: wmoerner@stanford.edu.

See Author Summary on page 18577.

This article contains supporting information online at www.pnas.org/lookup/suppl/doi:10.1073/pnas.1114444108/-DCSupplemental.

studies of *C. crescentus* thus far have been constrained by the use of two-dimensional (2D) superresolution microscopy, and extending these studies to 3D is necessary to reveal the true spatial relationships between these biological structures.

A natural extension to these studies is the colocalization of proteins relative to other cellular features within *C. crescentus*. Relative distances between proteins, for example, can reveal details about their dynamic interaction. Colocalization is often accomplished via multicolor imaging of photoactivatable fluorescent molecules, which requires multiple collinear imaging lasers creating alternating activation and imaging pulses (26, 27). Furthermore, the choice of fluorescent molecules is restricted, as the activation and emission spectra of each molecule must be carefully evaluated to minimize crosstalk. Samples must also be shielded from ambient light until they are imaged. In the case of fluorescent proteins, multicolor imaging requires the stable transfection of at least two fluorescent protein fusions, and additional controls must be performed to ensure that biological processes are unaffected by both fusions.

Here, we describe a method for sequential localization of an internal protein superstructure and the bacterial surface, termed superresolution by power-dependent active intermittency and points accumulation for imaging in nanoscale topography (SPRAIPAINT), which is a combination of photo-induced blinking of eYFP (SPRAI) and transient labeling of the cell surface via PAINT (9, 10). This method features the advantages of requiring a single reading laser, and PAINT can be performed indefinitely because of the continuous replenishment of dye from solution. The experimental setup and sample preparation are simple compared to multicolor photoactivation and photoswitching imaging experiments. Moreover, the use of wide field imaging techniques instead of spatial patterning of the excitation beam allows a large field of view to be imaged in 3D simultaneously. Combining this technique with the 3D imaging capabilities of the double-helix PSF (DH-PSF) (15, 20), we show remarkable 3D superresolution images of Crescentin-eYFP (CreS-eYFP), a cytoskeletal protein fusion, colocalized with the cell surface of live *C. crescentus*. The blinking behavior and localization characteristics of CreS-eYFP are also characterized. Furthermore, we analyze the spatial and temporal properties of cell surface localizations via PAINT. Finally, the generality of this imaging approach is demonstrated by replacing the standard PAINT dye, Nile red, with a unique dicyanomethylenedihydrofuran (DCDHF) derivative (28) and characterizing the spatial properties of the resulting reconstruction. To our knowledge, this demonstration of 3D superresolution imaging of intracellular protein superstructures colocalized with the surface of living cells has not been reported previously.

Results

Three-Dimensional SPRAIPAINT. To image protein superstructures relative to their biological context, the SPRAIPAINT concept (Fig. 1A, *Inset*) is based upon the idea of imaging two different fluorophores sequentially with only a single pumping laser and no need for a photoactivation laser. In other, more conventional SMACM methods such as PALM (5), FPALM (6), and STORM (8), the active fluorophore concentration must be controlled by some other mechanism to achieve PSF isolation and superlocalization (29, 30). In the SPRAI portion of our technique, eYFP is made to blink reversibly by driving the molecules into a dark state with simple high intensity laser pumping (25). During PAINT (9), fluorophores in solution dynamically bind to and unbind from the cellular membrane. As the bound form of the fluorophore is bright compared to the form in solution, single molecules on the surface can be preferentially imaged as required. In our experiments, we immobilized live *C. crescentus* cells expressing CreS-eYFP (Fig. 1A, *Inset*). In the first stage of imaging (SPRAI), we imaged and localized blinking single eYFP molecules until the population irreversibly photobleached. Next, we

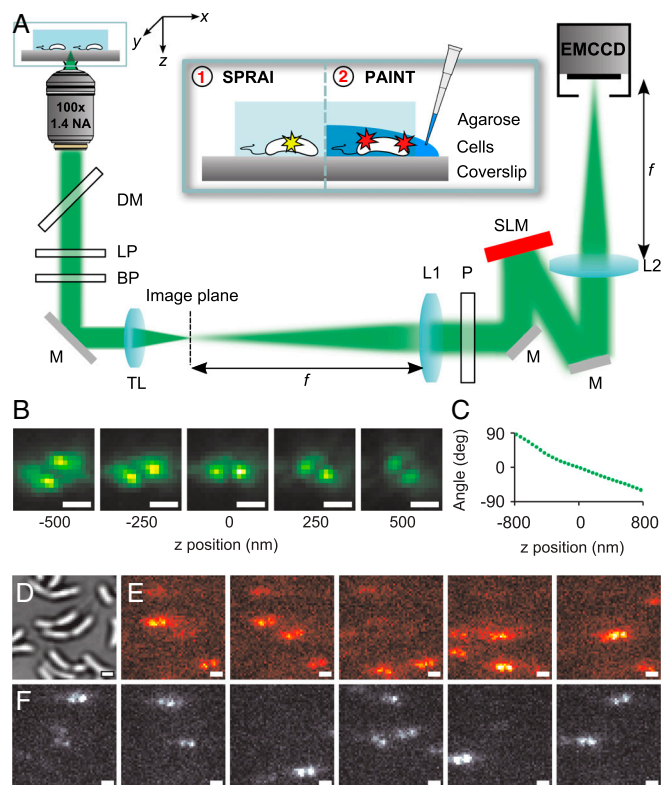


Fig. 1. Three-dimensional SPRAIPAINT concept. (A) Schematic of fluorescence detection path in the DH-PSF microscope. *Inset* shows SPRAIPAINT procedure. DM, dichroic mirror; LP, long pass filter; BP, band-pass filter; M, mirror; TL, tube lens; L1 and L2, lenses in $4f$ imaging system; P, polarizer; SLM, spatial light modulator; EMCCD, electron-multiplying charge-coupled device. (B) Images of the DH-PSF for various z positions of a fluorescent bead. (C) Calibration curve of angle versus z position for the DH-PSF, sampled every 50 nm. (D) Transmission white-light image of several *C. crescentus* cells during SPRAIPAINT imaging. (E) Raw DH-PSF fluorescence images of blinking eYFP during SPRAI imaging and (F) Nile red PAINT, both of the same field of view as D. Scale bars, 1 μm .

introduced a PAINT dye to the sample whose absorption was resonant with the same excitation source and imaged single molecules until a sufficient number of localizations were collected to effectively define the complex *Caulobacter* cell surface.

Three-dimensional superresolution information was collected by optically convolving the single-molecule images with the double-helix point spread function (Fig. 1A) (20, 31, 32). The DH-PSF converts the normal fluorescence spot of a single molecule into two spots by processing the image with a specially designed phase mask on a spatial light modulator. The DH-PSF imaging system encodes different z positions as different angles of the line between the two spots (Fig. 1B). For different axial positions, the two spots rotate about one another over a 1.6- μm range (Fig. 1C), creating a double helix along the z axis.

During our experiments, we observed *C. crescentus* cells in various stages of the cell cycle (Fig. 1D). For each field of view, we measured approximately 15,000 frames of eYFP blinking before photobleaching (Fig. 1E), with a 50-ms integration time and a mean background of 2.1 photons/pixel in each frame. This mean background increased to 4.0 photons/pixel per frame (30 ms exposure time) when imaging Nile red on the cell surface (Fig. 1F), consistent with a high concentration (3.5 nM) of freely diffusing fluors in the aqueous surroundings. We collected approximately 25,000 frames of Nile red PAINT data from each field of view, and the total SPRAIPAINT imaging time lasted approximately 20 min. To maximize localization precision, the exposure times were chosen such that most of the observed single

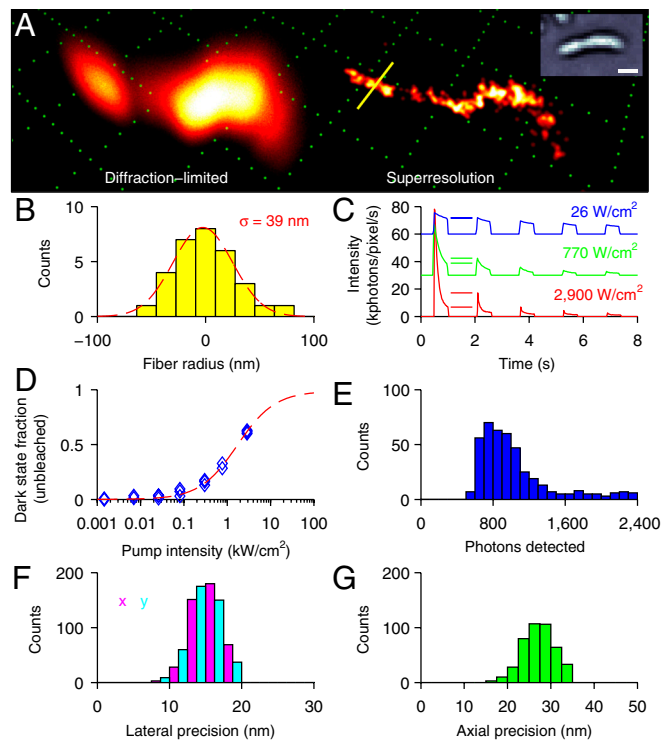


Fig. 3. Characterization of eYFP SPRAI imaging. (A) Diffraction-limited and superresolution 3D perspective images of a CreS-eYFP structure within *C. crescentus* generated using 431 localizations of eYFP. *Inset* shows a transmission white-light image of the same cell. Grid and scale bar, 1 μm . (B) Spatial distribution of eYFP within 150 nm of the yellow line shown in A. A Gaussian fit to the distribution shows a measured fiber thickness of 39 nm. (C) Measured intensity of bulk CreS-eYFP inside *C. crescentus* with pulsed excitation (0.5 s on time, 1 s off time) at various pump intensities (blue, 26 W/cm^2 ; green, 770 W/cm^2 ; red, 2.9 kW/cm^2). The blue and green curves are shifted upward by 60 and 30 kphotons/pixel/s, respectively, to enhance readability. The number of molecules recovered from the dark state during the first cycle is denoted by horizontal lines. (D) Fraction of unbleached molecules in the reversible dark state, as measured between the first and second pulses denoted in C, as a function of pump intensity. Dashed red line shows the fit to that of a three-level system with a long-lived dark state. (E) Distribution of photons detected from single eYFPs in the cell shown in A. (F) Distribution of lateral localization precision computed from the photon distribution in E. (G) Distribution of axial localization precision computed from the photon distribution in E.

is readily observable in our 3D superresolution images (Fig. 3A and *Movies S1–S4*). By drawing a line perpendicular to the fiber and binning molecule localizations within a 150 nm radius of the line, we measure the distribution shown and extract a fiber radius of approximately 39 nm (standard deviation, Fig. 3B). Because this CreS-eYFP fusion is expressed above the native background of the endogenous CreS population, the thickness of the fiber may be influenced somewhat by presence of the eYFP fusion. It is clear that the same underlying principles and methods could be applied to any other quasi-static protein superstructure of interest.

During our imaging experiments, the active control mechanism for eYFP was blinking, induced by the reading light. This blinking behavior is essential for superresolution microscopy, as the active emitter concentration must be reduced so that the individual single-molecule PSFs do not overlap. In the first report of single-molecule imaging of eYFP (35), both blinking and blue-light-induced rescue from a long-lived dark state were reported. In a previous study, a blue laser (405 nm) was used to reactivate eYFP protein fusions that had entered a long-lived dark state (11). Spontaneous return from a dark state was observed in several recent superresolution studies using eYFP without the need

for a blue reactivating laser (24, 25). Here, we characterized the blinking mechanism of eYFP by measuring the fluorescence of the CreS-eYFP fusions as a function of pumping power in a region containing many living cells. We pulsed the pumping laser with a mechanical shutter (on time = 0.5 s, off time = 1 s) and measured the fluorescence decay for three separate samples at each power level (1.4 W/cm^2 to 2.9 kW/cm^2). At high pumping intensities, a larger fractional portion of the eYFP population was observed to return from an inaccessible dark state, signified by a spike in fluorescence intensity after each off cycle (Fig. 3C). For shorter off times, the degree of recovery was reduced, suggesting a dark state lifetime on the order of hundreds of milliseconds. The fractional degree of fluorescence recovery increased dramatically with higher pumping intensities. The fraction of unbleached molecules shelved into the reversible dark state can be computed by measuring the fluorescence intensity before and after the first off cycle, such that

$$\frac{N_{\text{dark}}}{N_{\text{unbleached}}} = \frac{I_{2,\text{start}} - I_{1,\text{end}}}{I_{2,\text{start}}}, \quad [1]$$

where $I_{1,\text{end}}$ is the fluorescent intensity recorded at the end of the initial excitation pulse and $I_{2,\text{start}}$ is the fluorescent intensity recorded at the beginning of the second pulse. For a pumping intensity of 26 W/cm^2 , the dark state fraction was measured to be 0.02 ± 0.02 . However, for 770 W/cm^2 and 2.9 kW/cm^2 , we measured the fraction of molecules in the dark state to be 0.31 ± 0.03 and 0.62 ± 0.01 , respectively. The measured dark state fraction versus pumping power curve (Fig. 3D) fits the well-known behavior of a three-level system with a long-lived dark state ($R^2 = 0.99$) (36–38), which is given by

$$\frac{N_{\text{dark}}}{N_{\text{unbleached}}} = \frac{AI_{\text{pump}}}{(A+B)I_{\text{pump}} + C}, \quad [2]$$

where I_{pump} is the intensity of the excitation laser and A , B , and C are fitting parameters. This analysis confirms the existence of a long-lived, reversible dark state in eYFP, where the time-averaged probability of occupation of the dark state is dependent upon the reading power. It is important to note that, in addition to dark state shelving, photobleaching increases with pumping power, and thus, the pumping intensity must be chosen carefully to balance photobleaching and dark state shelving to achieve a desired number of localizations within a certain imaging time. (For the SPRAI imaging experiments shown here, we used a pumping intensity of 450 W/cm^2 .) The dark state does not appear to be a simple triplet state because the recovery time is longer than most triplet lifetimes, and may arise from reversible photophysics or photochemistry such as isomerization or hydrogen bond rearrangements. A more detailed photophysical analysis of eYFP is reserved for further study.

In our SPRAI imaging with eYFP, we measured approximately 1,000 photons detected per localization on average (Fig. 3E), although some molecules emitted significantly more photons. This number of photons corresponds to 15 nm localization precision in the lateral dimensions (Fig. 3F) and 27 nm localization precision in the axial dimension (Fig. 3G) using the previously measured scaling behavior of the DH-PSF (20).

Although SPRAIPAIN has the ability to resolve two-color 3D superresolution images in live bacterial cells with a single excitation source, as implemented here it is currently not suitable for every 3D biological sample. One of the shortcomings is the intrinsic sampling loss associated with the irreversible photobleaching of eYFP. Because the intense laser excitation does not drive all the fluorophores into the reversible long-lived dark state, some are irreversibly lost because of photobleaching (Fig. 3C). This loss will therefore decrease the number of single-molecule

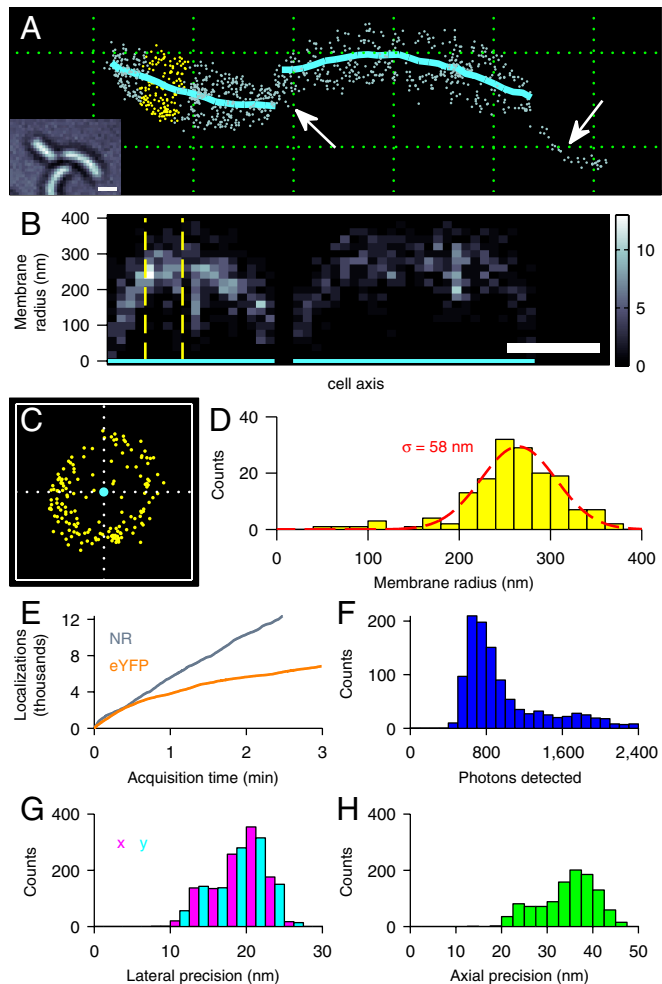


Fig. 4. Characterization of Nile red PAINT. (A) Scatter plot of 1,097 PAINT localizations of the *C. crescentus* cell surface (gray). These localizations clearly resolve the division septum and cell stalk (white arrows) and were used to compute the location of the cell's central axis (cyan). Inset shows transmission white-light image of the cell. Grid and scale bar, 1 μm . (B) Distribution of measured membrane radii as a function of distance along the cell. Scale bar, 1 μm . (C) Cross-section of PAINT localizations of the yellow slice of cell surface shown in A and B. Outer box, 1 \times 1 μm . (D) Distribution of measured radii for the yellow slice of membrane shown in A–C. Fitting the distribution to a Gaussian shows a measured thickness of 58 nm. (E) Cumulative number of Nile red PAINT localizations (gray) compared to eYFP SPRAI localizations (orange) versus acquisition time in a 30 \times 30 μm field of view. Plotted data corresponds to 5,000-frame acquisitions. (F) Distribution of photons detected from Nile red for the cell shown in A. (G) Distribution of lateral localization precision computed from the photon distribution in F. (H) Distribution of axial localization precision computed from the photon distribution in F.

localizations available to sample the superresolution structure. This drawback could be potentially solved by switching to a photoactivatable fluorescent protein [e.g., Dendra2, mEos2, or PA-mCherry (39–41)]; however, these systems present their own experimental challenges, for example, the need for a collinear switching laser in addition to the reading laser.

Characterization of Nile Red PAINT. The ability to colocalize intracellular proteins with respect to the cell surface depends on the labeling characteristics of the PAINT fluorophore. Here, we used our 3D localizations of Nile red to sense the surface of *C. crescentus*. The PAINT image shows that Nile red labels the surface with high specificity (Fig. 4A and Movies S1–S3). In particular, the division septum and stalk of the cell are highly resolved. In addition, the sampling of the surface is approximately uniform

across the entire cell. Assuming the cross-section of the cell to be approximately circular, we computed the location of the central axis along the cell's entire length. The radial distance from this axis to each of the PAINT localizations was calculated as a function of location along the cell's axis (Fig. 4B). This analysis reveals that a majority of the Nile red localizations occur on the cell surface and relatively few molecules localize inside the cell. We measure a characteristic cell diameter of approximately 500–600 nm, which is consistent with previous studies of *Caulobacter* (42–44). In addition, we isolated a 400-nm thick axial slice of the surface, and as expected, these localizations reveal that the membrane cross-section is approximately circular (Fig. 4C), with the preponderance of localizations residing on the surface rather than in the cytoplasm.

By binning the radii of these localizations, we measured a mean membrane radius of 270 nm and a membrane thickness of 58 nm (standard deviation, Fig. 4D). This thickness is larger than the precision predicted by the number of detected photons and can be attributed to a number of factors. First, the binding kinetics of Nile red molecules on living cell membranes are not well understood, and Nile red may emit fluorescence not only in the outer or inner membrane but also when interacting with the cell wall. Secondly, because of the imperfect nature of the live-cell gel immobilization technique, nanoscale movements of the live bacteria relative to the fiducial marker may cause broadening. Finally, single-molecule dipole orientation effects could introduce an error (45), depending on the orientational mobility of emitting Nile red molecules.

Photobleaching, which normally limits the number and precision of single-molecule localizations during SMACM, is not an issue during PAINT because of the continuous supply of new emitters from the solution, and this property is a defining characteristic of the technique. This replenishment is evidenced by the number of PAINT single-molecule localizations we detect as a function of time (Fig. 4E). During the first 5,000-frame acquisition, the cumulative number of SPRAI localizations of eYFP approaches an asymptote as the sample is imaged, which shows that photobleaching limits the total number of single-molecule localizations of eYFP. In contrast, the number of PAINT localizations increases linearly with time, once the concentration of PAINT dye reaches equilibrium after being added to the sample. This localization rate is a defining signature of the PAINT technique.

Furthermore, we measured the number of photons detected per localization versus acquisition time for both eYFP and Nile red (Fig. S3). There is a slight decay in the number of photons detected from eYFP as the experiment progressed, but the number of photons detected from Nile red is essentially constant throughout the entire experiment. This result demonstrates that photobleaching is the primary limitation for SPRAI imaging of eYFP, whereas Nile red can be imaged almost indefinitely during PAINT.

With an average of 1,000 photons detected per localization (Fig. 4F), our mean precision with Nile red PAINT is 19 nm in the x and y directions (Fig. 4G) and 34 nm in the z direction (Fig. 4H). Even though we detect approximately the same number of photons from eYFP and Nile red, our background when imaging Nile red was higher, thereby causing our localization precision with Nile red to be worse.

Three-Dimensional SPRAI PAINT Using eYFP and DCDHF-Tail. DCDHF chromophores have been demonstrated to be useful single-molecule labels with beneficial properties such as viscosity-dependent fluorescence and strong solvatochromism (46, 47). This interesting family of fluorophores has been shown to provide many imaging functionalities by chemical derivatization (48). With long-chain alkyl substituents, DCDHFs can be synthesized with amphiphilic properties and can therefore in principle label

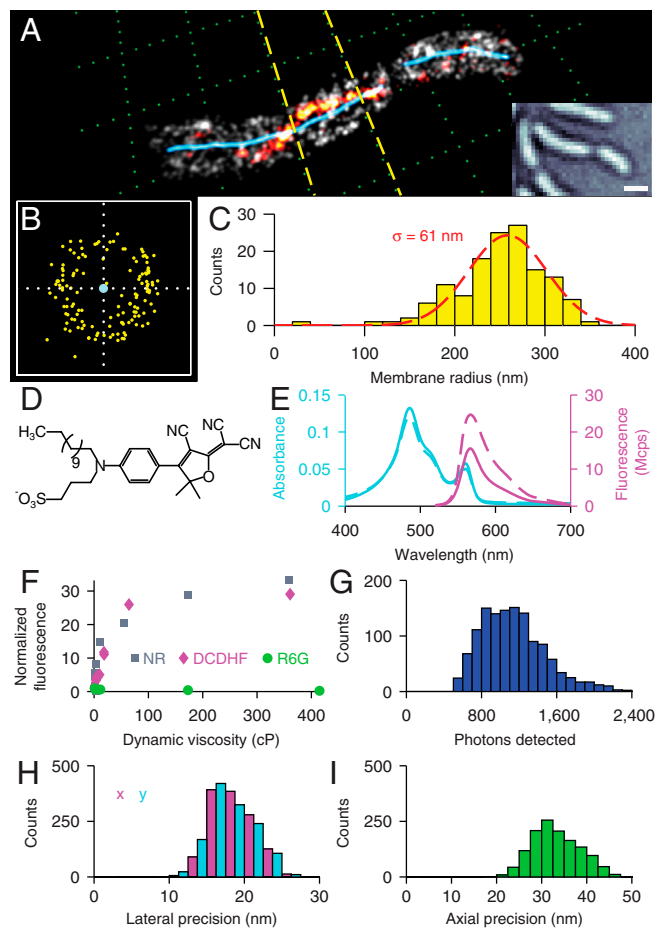


Fig. 5. Three-dimensional SPRAIPAIN using eYFP and DCDHF-tail. (A) Three-dimensional SPRAIPAIN image of CreS-eYFP (395 localizations, red-orange) and DCDHF-tail (1,291 localizations, gray). PAIN localizations were used to compute the location of the cell's central axis (cyan). *Inset* shows a transmission white-light image of the cell. Grid and scale bar, 1 μm . (B) Cross-section of PAIN localizations of the yellow slice of cell membrane shown in A. Outer box, 1 μm . (C) Distribution of measured radii for the yellow slice of membrane shown in A and B. Fitting the distribution to a Gaussian shows a measured thickness of 61 nm. (D) Chemical structure of DCDHF-tail. (E) Absorbance and fluorescence of DCDHF-tail in PBS with (dashed line) and without (solid line) *C. crescentus* cells. (F) Normalized fluorescence versus viscosity for Nile red (gray squares), DCDHF-tail (magenta diamonds), and Rhodamine 6G (green circles). (G) Distribution of photons detected from DCDHF-tail for the cell shown in A. (H) Distribution of lateral localization precision computed from the DCDHF-tail photon distribution in G. (I) Distribution of axial localization precision computed from the DCDHF-tail photon distribution in G.

aliphatic cell membranes (49). To demonstrate the broad usefulness of SPRAIPAIN and verify the cell surface imaging by Nile red, we performed 3D SPRAIPAIN on *C. crescentus* using an amphiphilic DCDHF derivative, henceforth referred to as DCDHF-tail (Fig. 5D) (28).

A 3D SPRAIPAIN image using eYFP and DCDHF-tail shows that DCDHF-tail also labels the cell membrane with high specificity (Fig. 5A and *Movie S4*). The sampling of the cell membrane is roughly uniform, and the division septum is clearly resolved in the image. Similar to the Nile red measurements, we computed the location of the cell's central axis, and by isolating a 1- μm axial slice of membrane, we found that the measured membrane cross-section using DCDHF-tail is also approximately circular (Fig. 5B). By binning the PAIN localization radii for this slice, we measured a membrane radius of 260 nm and a thickness of 61 nm (standard deviation, Fig. 5C). Again, this thickness is larger than that measured by electron microscopy and is likely

attributable to the aforementioned factors that affect Nile red PAIN.

To characterize DCDHF-tail (Fig. 5D) as a PAIN dye, we measured its absorption and fluorescence spectra in PBS buffer with and without *C. crescentus* cells (Fig. 5E). DCDHF-tail's absorption is unaffected by adding cells to the buffer. However, we measure a 1.8-fold increase in integrated fluorescence intensity when adding cells to the DCDHF-tail solution. This increase is most likely because of DCDHF-tail's strong viscosity-dependent emission, which causes an increase in fluorescence intensity as large as 30-fold in glycerol versus water (Fig. 5F). This viscosity dependence is extremely beneficial for PAIN, as it increases the effective turn-on ratio of the molecule. As a comparison, the fluorescence of Nile red exhibited a similar increase but Rhodamine 6G did not show any increase with viscosity, and therefore, in this regard both Nile red and DCDHF-tail are more suitable PAIN dyes.

With an average value of 1,100 photons detected per localization (Fig. 5G), our mean precision with DCDHF-tail PAIN is 18 nm in the x and y directions (Fig. 5H) and 33 nm in the z direction (Fig. 5I). The mean background during these measurements was 5.1 photons/pixel per frame. The PAIN imaging conditions used for DCDHF-tail were identical to those used for Nile red, and it is possible that with further optimization, the additional photons available from DCDHF-tail can be used to achieve even higher localization precision.

Discussion

It is important to understand the factors that are used to optimize good PAIN fluorophores in order to develop future probes. Nile red has been used almost exclusively in PAIN experiments (9, 10) for many reasons, including: its specificity to the cell surface and not the substrate, its viscosity-dependent fluorescence emission (sometimes called membrane sensing), its excellent turn-on ratio, and its spectral shift of absorption during binding. In addition, its lack of charge aids its solubility in both polar and lipid environments, where a careful tuning of the amphiphilic nature of the dye is required for optimal temporal binding kinetics (50). Fortunately, DCDHF-tail also displays the characteristics of a good PAIN dye, namely: an aliphatic region for membrane binding, charge to allow the molecule to remain outside the cell and to impart water solubility, and the push-pull DCDHF fluorophore moiety. In addition, this molecule also demonstrates excellent photophysical characteristics including: uniform labeling of the membrane (Fig. 5A), a strong increase in fluorescence emission in more viscous environments comparable to that of Nile red (Fig. 5D), and an increased number of detected photons through the DH-PSF microscope as compared to Nile red (Fig. 5E). All these factors demonstrate that other molecules can be excellent candidates for PAIN imaging and warrant further investigation.

In these experiments, the binding of the PAIN dye is non-specific, allowing nonbiased sampling of the entire outer surface of the *C. crescentus* cell, where the number of localizations is linear with and limited only by the length of imaging time (Fig. 4E). Although this binding characteristic is useful in determining spatial positions of interior proteins relative to the cell surface, we propose that it may be possible to modify the dye so that it binds to specific regions of the membrane (10) (e.g., regions with high curvature or at lipid-partitioning regions). This approach can be explored with future rational fluorophore design. In the sample geometry demonstrated here, washing out the PAIN dye after adding it to the sample is not possible. However, incorporating the imaging in a microfluidic platform, for example, could facilitate the introduction and washing of the PAIN dye, as well as delivery of nutrients to the cells for longer-term imaging.

Notably, the SPRAIPAINT imaging strategy is independent of the 3D imaging method used to localize single molecules. Here, we utilized the DH-PSF for its excellent and uniform 3D localization precision across its whole depth of field (20, 51), but other 3D superresolution methods (14, 17) can be applied for 3D SPRAIPAINT as well. The choice of 3D method is largely influenced by the desired localization precision and depth of field required to image the target structure labeled with a candidate fluorophore. The DH-PSF has an operational depth of field of 2 μm , limited by the PSF design itself. If the target structure spans an axial range greater than 2 μm , the sample would need to be scanned axially (52) to use the DH-PSF for 3D SPRAIPAINT. Aberrations associated with imaging deeply into mismatched media would also need to be considered.

Three-dimensional SPRAIPAINT achieves colocalization via the sequential acquisition of intracellular protein locations followed by imaging of the cell surface, thereby simplifying the optical setup and biological sample preparation required versus typical two-color colocalization experiments using photoactivatable fluorophores. In addition, observing protein dynamics within single living cells relative to the cell surface is possible using the SPRAIPAINT technique. In the future, it is to be expected that SPRAIPAINT can be optimized to decrease the total amount of imaging time required to resolve complex 3D structures, modified by using PAINT dyes designed to light up specific desired regions of the cellular surface or membrane, and enhanced with additional optimized fluorescent proteins.

Methods

Bacterial Strains and Culture Conditions. To enable superresolution localization of fluorescently-tagged CreS molecules in *Caulobacter*, we created a xylose-inducible eYFP fusion to *creS* in the wild-type *Caulobacter* background. KOD Hot Start DNA Polymerase (Novagen) was used to PCR amplify the *Caulobacter creS* gene from genomic DNA using the primers GCATCACA-TATG CAGCACCAGATCGAGTCCAC and GCATCAGAGCTCGGGCGCTCGCGGC-CAGTCCGCGTC, which add a 5' NdeI and in frame 3' SacI site to the product (underlined). This amplified fragment and the plasmid pXYFPC-5 (53) were digested with NdeI and SacI, and the vector was dephosphorylated using Calf Intestinal Phosphatase (New England BioLabs, Inc.) before gel purification and ligation using T4 DNA ligase (Fermentas). The correct plasmid, pJP124, was sequence verified. The plasmid pJP124 was introduced into wild-type *Caulobacter* CB15N via electroporation and integrated at the *xyiX* chromosomal locus. The resulting strain, JP198, contained a xylose-inducible *creS-eYFP* gene at *xyiX* in addition to the untagged *creS* gene at the native chromosomal locus.

Sample Preparation for Single-Molecule SPRAIPAINT Imaging. Asynchronous cultures of *C. crescentus* strain JP198 were grown in minimal growth media (M2G) at 28 °C for 2 d at log phase, induced with 0.03% xylose for 90 min. The culture was washed by centrifugation (8,000 rpm for 3 min) and resuspension in clean cold M2G three times, before a final suspension in pH 7.4 PBS buffer (Gibco). One microliter of cells was mounted on a $\sim 5 \times 5 \times 2$ mm pad of 2% agarose (Sigma) in M2G, which was mounted in the center of a 25 \times 25 mm glass slide (Fisher Finest, No. 1) and imaged immediately and only once before being discarded. Fluorescent beads (2 pM in PBS) were added (565/580 carboxylate-modified FluoSpheres, Molecular Probes, 100 nm) as fiduciary markers.

Single-Molecule SPRAIPAINT Imaging. The double-helix 3D microscope uses a 4f imaging system ($f = 15$ cm) to relay the fluorescence image from an inverted microscope (Olympus IX71) onto an electron-multiplying charge-coupled camera (Andor Ixon⁺ DU-897E) (Fig. 1A). The imaging system convolves the standard PSF of the microscope with the DH-PSF using a phase-only spatial light modulator (Boulder Nonlinear Systems XY phase series) and has been described previously in detail (20, 32, 54). For this study, we illuminated *C. crescentus* cells with 514-nm light (Coherent Innova 90 Ar⁺ laser). The fluorescence from the sample was collected by a 100 \times 1.4 N.A. oil-immersion objective (Olympus UPlanSApo 100 \times /1.40) and filtered through a dichroic mirror (Chroma, Z514RDC) and a 530-nm long pass filter (Omega XF3082). During imaging, the focal plane of the microscope was positioned near the axial midplane of the cells. In addition, the excitation beam was tilted at an angle with respect to the optical axis; this pseudo-total

internal reflection fluorescence configuration reduced the background fluorescence during imaging. The size of the excitation spot was 30 μm ($1/e^2$ radius).

Imaging was performed sequentially with the genetically encoded fluorescent protein imaged first (SPRAI imaging) until near complete photobleaching was observed, then the nonspecific PAINT dye was added and allowed to quickly diffuse through the (intentionally) small agarose pad.

For SPRAI imaging, we illuminated the sample at a peak intensity of 450 W/cm² (calibrated by taking into account the shape of the background fluorescence created by the excitation spot), used an additional 535/70 band-pass filter (Chroma HQ535/70 M), and acquired the data with a 50 ms exposure time. The use of eYFP required initial bleaching and shelving of fluorophores into the dark state by the illumination laser until separated single molecules were observed. Imaging continued until few molecules were observed returning from the dark state ($\sim 15,000$ frames).

For PAINT, we used a peak intensity of 1.1 kW/cm², filtered the emission with a 590/60 band-pass filter, and imaged the single molecules with a 30 ms integration time. The PAINT dye was introduced by pipetting 20 μL of dye solution (3.5 nM of Nile red or 2.2 μM of DCDHF-tail in PBS buffer) onto the coverslip near the agarose pad. The cell positions were monitored by white light to ensure minimal sample perturbation while the dye was deposited, with the fiduciary markers providing confirmation. PAINT imaging began immediately after dye deposition and continued for 25,000 frames.

Power intensities were experimentally optimized in an attempt to maximize the signal-to-background ratio, and hence the localization precision, in each imaging frame. The precise effect of intensity upon precision is controlled by various fluorophore-dependent parameters (e.g., binding kinetics of the PAINT fluorophore, dark state shelving kinetics).

SPRAIPAINT Image Analysis. The 3D positions of single molecules exhibiting the DH-PSF were analyzed using custom software written in MATLAB (MathWorks, SI Text). In brief, the code identifies images of the DH-PSF within each frame of fluorescence data using known templates (Fig. S4) and then fits each of them to a double Gaussian function (Fig. S5). The lateral xy position of a single molecule is computed from the midpoint between the two fitted Gaussians, and the axial z position is computed from the angle of the line between the two Gaussians relative to a fixed horizontal line using a calibration curve (Fig. 1C). Lateral shift of the DH-PSF as a function of z position is also removed using a similar calibration curve (Fig. S6). Drift correction was applied to each localization by tracking the movements of 2–3 fiduciary beads within the field of view (Fig. S7 and SI Text). The precision of each localization was computed directly from the number of photons detected and the measured background (20) (SI Text).

The calibration curve was measured by imaging fluorescent beads (565/580 carboxylate-modified FluoSpheres, Molecular Probes, 100 nm) in agarose gel. The rotation and translation of the DH-PSF was measured while translating the objective lens in 50-nm steps along the z -direction using a piezoelectric objective scanner (Physik Instrumente PIFOC P-721.CDQ with E-625.CO controller). More details on the calibration of the DH-PSF imaging system can be found in previous work (20, 54).

Because of the index mismatch between immersion oil ($n = 1.518$) and *C. crescentus* cells ($n \approx 1.3$), the true z position of a fluorescent molecule differs from the measured z position in our experiments (55, 56). Because we place the focal plane of the microscope approximately 300 nm from the glass-water interface and image single molecules within 300 nm of this focal plane, the focal shift is mostly linear (52, 57). We therefore use a z correction factor of $n_{\text{water}}/n_{\text{oil}} = 0.88$ to convert measured z positions to true z positions, and this correction factor is accurate enough to produce circular membrane cross sections in our 3D data (Fig. 4C and Fig. 5B). A more precise correction factor may be required if measurements are taken further away from the glass-water interface.

The location of each cell's central axis was computed using a custom MATLAB script (SI Text). Briefly, the 3D PAINT localizations from each individual cell were isolated and rotated to align as closely as possible with the x axis. The localizations were then separated into transverse yz slices along the x axis (300-nm thick, sampled every 100 nm). In each slice, the best position for the cell's central axis was calculated by minimizing the standard deviation of the distances between the best center position and each localization in the slice. By sectioning the PAINT localizations in this manner, a smooth representation of the cell's central axis was readily obtained (Fig. 4A and Fig. 5A).

The superresolution images are the sum of all fitted positions, where the long integration times of 30 ms and 50 ms rejected quickly diffusing molecules. When plotting data from individual cells, localizations from nearby cells were removed for clarity. All scatter plots used 20-nm diameter circles to plot localizations. Two-dimensional projections of 3D data were plotted

using a custom macro written in ImageJ (<http://rsb.info.nih.gov/ij/>). Each localization was plotted as an identical 2D Gaussian spot with a width σ of 20 nm. Three-dimensional perspective renders were generated using a custom script written in MATLAB. Again, each localization was plotted as an identical 3D Gaussian spot with width σ of 20 nm. For simulating the diffraction-limited 3D PSF, each localization was plotted as an identical 3D Gaussian spot with widths $\sigma_x = \sigma_y = 100$ nm and $\sigma_z = 400$ nm.

Photophysical Measurements of Nile Red, DCDHF-Tail, and Rhodamine 6G.

The shift in absorbance and emission of DCDHF-tail in PBS upon addition of wild-type *C. crescentus* cells was measured on a Cary 6000i UV-visible-near infrared spectrophotometer (Varian) and a Fluorolog 3 (Jobin-Yvon Horiba) fluorimeter with an excitation wavelength of 480 nm and standard 1-cm path length cuvettes. The cells and dye were incubated for 10 min to ensure equilibrium was reached. Final spectra subtract the absorbance and emission from the cells only.

The effect of viscosity on the fluorescence from DCDHF-tail, Nile red and Rhodamine 6G was quantified by measuring the emission spectra in varying glycerol-water mixtures. Emission spectra were measured on a FluoroMax-4 spectrofluorometer (Jobin-Yvon Horiba), with excitation at 480 nm and the same OD of fluorophore. The OD was kept below 0.1 to avoid inner filter effects. The integrated fluorescence areas were normalized by the total fluorescence in water.

The dynamic viscosity of the glycerol-water mixtures was estimated using the following procedure (58). Briefly, the dynamic viscosity μ [centipoise (cP)

or 0.001 Ns/m²] is related to the two component viscosities in power form:

$$\mu = \mu_w^\alpha \mu_g^{1-\alpha} = \mu_g \exp(A\alpha), \quad [3]$$

where μ_g is the viscosity of glycerol, μ_w is the viscosity of water, and $A = \ln(\mu_w/\mu_g)$. In addition,

$$\alpha = \frac{\ln(\mu/\mu_g)}{\ln(\mu_w/\mu_g)} \approx 1 - C_m + \frac{abC_m(1 - C_m)}{aC_m + b(1 - C_m)}, \quad [4]$$

where C_m is the glycerol concentration in mass, and a and b are temperature-dependent coefficients, empirically given by $a = 0.705 - 0.00177T$, $a = 0.705 - 0.00177T$, and $b = (4.9 + 0.036T)a^{2.5}$. At 20 °C, $\mu_w = 1.0049$ cP and $\mu_g = 1,413.8$ cP.

ACKNOWLEDGMENTS. We acknowledge R. Piestun for providing the DH-PSF phase mask design. We thank Dr. Randall Goldsmith and Michael Thompson for helpful discussions and Scott Hsieh for assistance with the double helix fitting and visualization code. This work was supported by National Institute of General Medical Sciences Grants R01GM085437 (to W.E.M.), R01GM032506 (to L.S.), and R01GM086196 (to W.E.M., R.J.T., and L.S.), a National Science Foundation Graduate Research Fellowship and 3Com Corporation Stanford Graduate Fellowship (M.D.L.), and a National Institutes of Health/National Institute of General Medical Sciences Fellowship F32GM088966-2 (to J.P.).

- Larabell CA, Le Gros MA (2004) X-ray tomography generates 3-D reconstructions of the yeast, *Saccharomyces cerevisiae*, at 60-nm resolution. *Mol Biol Cell* 15:957–962.
- Hohmann-Marriott M, et al. (2009) Nanoscale 3D cellular imaging by axial scanning transmission electron tomography. *Nat Methods* 6:729–731.
- Schermelleh L, et al. (2008) Subdiffraction multicolor imaging of the nuclear periphery with 3D structured illumination microscopy. *Science* 320:1332–1336.
- Donner G, et al. (2006) Macromolecular-scale resolution in biological fluorescence microscopy. *Proc Natl Acad Sci USA* 103:11440–11445.
- Betzig E, et al. (2006) Imaging intracellular fluorescent proteins at nanometer resolution. *Science* 313:1642–1645.
- Hess ST, Girirajan TPK, Mason MD (2006) Ultra-high resolution imaging by fluorescence photoactivation localization microscopy. *Biophys J* 91:4258–4272.
- Heilemann M, et al. (2008) Subdiffraction-resolution fluorescence imaging with conventional fluorescent probes. *Angew Chem Int Ed* 47:6172–6176.
- Rust MJ, Bates M, Zhuang X (2006) Sub-diffraction-limit imaging by stochastic optical reconstruction microscopy (STORM). *Nat Methods* 3:793–795.
- Sharonov A, Hochstrasser RM (2006) Wide-field subdiffraction imaging by accumulated binding of diffusing probes. *Proc Natl Acad Sci USA* 103:18911–18916.
- Kuo C, Hochstrasser RM (2011) Super-resolution microscopy of lipid bilayer phases. *J Am Chem Soc* 133:4664–4667.
- Biteen JS, et al. (2008) Super-resolution imaging in live *Caulobacter crescentus* cells using photoswitchable EYFP. *Nat Methods* 5:947–949.
- Folling J, et al. (2008) Fluorescence nanoscopy by ground-state depletion and single-molecule return. *Nat Methods* 5:943–945.
- Steinhauer C, Forthmann C, Vogelsang J, Tinnefeld P (2008) Superresolution microscopy on the basis of engineered dark states. *J Am Chem Soc* 130:16840–16841.
- Huang B, Wang W, Bates M, Zhuang X (2008) Three-dimensional super-resolution imaging by stochastic optical reconstruction microscopy. *Science* 319:810–813.
- Pavani SRP, et al. (2009) Three-dimensional, single-molecule fluorescence imaging beyond the diffraction limit by using a double-helix point spread function. *Proc Natl Acad Sci USA* 106:2995–2999.
- Lew MD, Lee SF, Badieirostami M, Moerner WE (2011) Corkscrew point spread function for far-field three-dimensional nanoscale localization of pointlike objects. *Opt Lett* 36:202–204.
- Juette MF, et al. (2008) Three-dimensional sub-100 nm resolution fluorescence microscopy of thick samples. *Nat Methods* 5:527–529.
- Tang J, Akerboom J, Vaziri A, Looger LL, Shank CV (2010) Near-isotropic 3D optical nanoscopy with photon-limited chromophores. *Proc Natl Acad Sci USA* 107:10068–10073.
- Mlodzianoski MJ, Juette MF, Beane GL, Bewersdorff J (2009) Experimental characterization of 3D localization techniques for particle-tracking and super-resolution microscopy. *Opt Express* 17:8264–8277.
- Thompson MA, Lew MD, Badieirostami M, Moerner WE (2010) Localizing and tracking single nanoscale emitters in three dimensions with high spatiotemporal resolution using a double-helix point spread function. *Nano Lett* 10:211–218.
- Shtengel G, et al. (2009) Interferometric fluorescent super-resolution microscopy resolves 3D cellular ultrastructure. *Proc Natl Acad Sci USA* 106:3125–3130.
- Aquino D, et al. (2011) Two-color nanoscopy of three-dimensional volumes by 4Pi detection of stochastically switched fluorophores. *Nat Methods* 8:353–359.
- Greenfield D, et al. (2009) Self-organization of the *Escherichia coli* chemotaxis network imaged with super-resolution light microscopy. *PLoS Biol* 7:e1000137.
- Ptacin JL, et al. (2010) A spindle-like apparatus guides bacterial chromosome segregation. *Nat Cell Biol* 12:791–798.
- Lee SF, Thompson MA, Schwartz MA, Shapiro L, Moerner WE (2011) Super-resolution imaging of the nucleoid-associated protein HU in *Caulobacter crescentus*. *Biophys J* 100:L31–L33.
- Bates M, Huang B, Dempsey GT, Zhuang X (2007) Multicolor super-resolution imaging with photo-switchable fluorescent probes. *Science* 317:1749–1753.
- Shroff H, et al. (2007) Dual-color superresolution imaging of genetically expressed probes within individual adhesion complexes. *Proc Natl Acad Sci USA* 104:20308–20313.
- Wang H, Lu Z, Lord SJ, Moerner WE, Twieg RJ (2007) Modifications of DCDHF single molecule fluorophores to impart water solubility. *Tetrahedron Lett* 48:3471–3474.
- Yildiz A, et al. (2003) Myosin V walks hand-over-hand: Single fluorophore imaging with 1.5-nm localization. *Science* 300:2061–2065.
- Kim SY, Gitai Z, Kinkhabwala A, Shapiro L, Moerner WE (2006) Single molecules of the bacterial actin MreB undergo directed treadmilling motion in *Caulobacter crescentus*. *Proc Natl Acad Sci USA* 103:10929–10934.
- Pavani SRP, Piestun R (2008) Three dimensional tracking of fluorescent microparticles using a photon-limited double-helix response system. *Opt Express* 16:22048–22057.
- Pavani SRP, Greengard A, Piestun R (2009) Three-dimensional localization with nanometer accuracy using a detector-limited double-helix point spread function system. *Appl Phys Lett* 95:021103.
- Ausmees N, Kuhn JR, Jacobs-Wagner C (2003) The bacterial cytoskeleton: An intermediate filament-like function in cell shape. *Cell* 115:705–713.
- Charbon G, Cabeen MT, Jacobs-Wagner C (2009) Bacterial intermediate filaments: In vivo assembly, organization, and dynamics of crescentin. *Genes Dev* 23:1131–1144.
- Dickson RM, Cubitt AB, Tsien RY, Moerner WE (1997) On/Off blinking and switching behavior of single green fluorescent protein molecules. *Nature* 388:355–358.
- Ambrose WP, Basché T, Moerner WE (1991) Detection and spectroscopy of single pentacene molecules in a p-terphenyl crystal by means of fluorescence excitation. *J Chem Phys* 95:7150–7163.
- Hell SW, Krug M (1995) Ground-state-depletion fluorescence microscopy: A concept for breaking the diffraction resolution limit. *Appl Phys B: Lasers Opt* 60:495–497.
- Schwille P, Kummer S, Heikal AA, Moerner WE, Webb WW (2000) Fluorescence correlation spectroscopy reveals fast optical excitation-driven intermolecular dynamics of yellow fluorescent proteins. *Proc Natl Acad Sci USA* 97:151–156.
- Gurskaya NG, et al. (2006) Engineering of a monomeric green-to-red photoactivatable fluorescent protein induced by blue light. *Nat Biotechnol* 24:461–465.
- McKinney SA, Murphy CS, Hazelwood KL, Davidson MW, Looger LL (2009) A bright and photostable photoconvertible fluorescent protein. *Nat Methods* 6:131–133.
- Subach FV, et al. (2009) Photoactivatable mCherry for high-resolution two-color fluorescence microscopy. *Nat Methods* 6:153–159.
- Poindexter JS (1964) Biological properties and classification of the caulobacter group. *Microbiol Mol Biol Rev* 28:231–295.
- Skerker JM, Laub MT (2004) Cell-cycle progression and the generation of asymmetry in *Caulobacter crescentus*. *Nat Rev Microbiol* 2:325–337.
- Laub MT, Shapiro L, McAdams HH (2007) Systems biology of caulobacter. *Annu Rev Genet* 41:429–441.
- Engelhardt J, et al. (2011) Molecular orientation affects localization accuracy in superresolution far-field fluorescence microscopy. *Nano Lett* 11:209–213.
- Willetts KA, Callis PR, Moerner WE (2004) Experimental and theoretical investigations of environmentally sensitive single-molecule fluorophores. *J Phys Chem B* 108:10465–10473.
- Willetts KA, Nishimura SY, Schuck PJ, Twieg RJ, Moerner WE (2005) Nonlinear optical chromophores as nanoscale emitters for single-molecule spectroscopy. *Acc Chem Res* 38:549–556.

48. Lord SJ, et al. (2010) Azido push-pull fluorogens photoactivate to produce bright fluorescent labels. *J Phys Chem B* 114:14157–14167.
49. Nishimura SY, et al. (2006) Diffusion of lipid-like single-molecule fluorophores in the cell membrane. *J Phys Chem B* 110:8151–8157.
50. Kim SY, et al. (2005) Probing the sequence of conformationally induced polarity changes in the molecular chaperonin GroEL with fluorescence spectroscopy. *J Phys Chem B* 109:24517–24525.
51. Badieirostami M, Lew MD, Thompson MA, Moerner WE (2010) Three-dimensional localization precision of the double-helix point spread function versus astigmatism and biplane. *Appl Phys Lett* 97:161103.
52. Huang B, Jones SA, Brandenburg B, Zhuang X (2008) Whole-cell 3D STORM reveals interactions between cellular structures with nanometer-scale resolution. *Nat Methods* 5:1047–1052.
53. Thanbichler M, Niesta AA, Shapiro L (2007) A comprehensive set of plasmids for vanillate- and xylose-inducible gene expression in *Caulobacter crescentus*. *Nucleic Acids Res* 35:e137.
54. Lew MD, Thompson MA, Badieirostami M, Moerner WE (2010) In vivo three-dimensional superresolution fluorescence tracking using a double-helix point spread function. *Proc SPIE* 7571:75710Z.
55. Hell SW, Reiner G, Cremer C, Stelzer EHK (1993) Aberrations in confocal fluorescence microscopy induced by mismatches in refractive index. *J Microsc* 169:391–405.
56. Neuman KC, Abbondanzieri EA, Block SM (2005) Measurement of the effective focal shift in an optical trap. *Opt Lett* 30:1318–1320.
57. Deng Y, Shaevitz JW (2009) Effect of aberration on height calibration in three-dimensional localization-based microscopy and particle tracking. *Appl Opt* 48:1886–1890.
58. Cheng N (2008) Formula for the viscosity of a glycerol-water mixture. *Ind Eng Chem Res* 47:3285–3288.

Supporting Information

Lew et al. 10.1073/pnas.1114444108

SI Text

Double-Helix Point Spread Function (DH-PSF) Automated Recognition and Fitting. The 3D locations of single molecules are extracted frame-by-frame from raw movies using an automated image-processing algorithm implemented in MATLAB. This algorithm contains two components: (i) a coarse recognition step, in which DH-PSFs are identified and localized with integer-pixel resolution, and (ii) a fine fitting stage, which fits each DH-PSF image identified above to a double-Gaussian model of the DH-PSF and produces 3D positions. The algorithm can fit approximately 15–20 molecules per second on an Intel Core 2 Duo workstation with 4 GB of RAM.

The coarse recognition algorithm uses template matching to identify DH-PSFs from raw data containing single molecules. Template matching is a process in which instances of a known template $t(x,y)$ are identified in an image $s(x,y)$ by selecting locations (p, q) that minimize the mean-squared error quantity

$$E(p,q) = \sum_x \sum_y [s(x,y) - t(x-p,y-q)]^2.$$

The minimization of the error quantity may be equivalently recast as the maximization of the area correlation, $r(p,q) = s(p,q) \otimes t(-p, -q)$. Because the convolution operation is computationally costly, this operation is performed in the Fourier domain as a simple multiplication.

Because the DH-PSF rotates as a function of the axial position of an emitter, several templates must be used to recognize all possible orientations of the DH-PSF. The templates used in the detection algorithm are taken from the fluorescent bead calibration movies measured at the same imaging conditions as the single-molecule data. Five templates were chosen, with the DH-PSF rotated approximately 30 degrees between each template (see Fig. S4). This number of templates represents a good balance between matching accuracy and computational speed.

Template matching with each of the templates is performed using phase correlation in the Fourier domain. Phase correlation normalizes the input image and template image amplitudes in the Fourier domain, thereby minimizing the bias of template matching to bright regions of the image. Before transforming to the Fourier domain, each template t_k is padded with zeros to match the size of the raw data. The phase correlation image r_k is then computed from the raw data s and the k th template with the formula

$$r_k = F^{-1} \left(\frac{F\{h\}F\{s\}F\{t_k\}^*}{|F\{s\}||F\{t_k\}|} \right),$$

where F denotes the two-dimensional Fourier transform, F^{-1} denotes the two-dimensional inverse Fourier transform, and the prefilter h is a Gaussian low pass filter with a width $\sigma = 1.5$ pixels. Because phase correlation emphasizes high frequency components (1) and these spatial frequencies typically have a lower signal to background ratio, the Gaussian low pass filter h is used to filter out these higher frequencies and thus leads to more robust template matches.

Local maxima (i.e., peaks) above a user-defined threshold are detected in each image r_k , and the locations and magnitudes of each peak are stored in memory. Because the peak threshold is set low enough to detect weak single molecules, extraneous matches occur for brighter single molecules. If the candidate DH-PSF is bright enough, a template will match at locations

where only one of its spots overlaps with only one of the spots in the input image. These ghost matches are filtered out by enforcing a minimum distance between all of the template matches in a given frame of the input data. This minimum distance is chosen to be the typical diameter of the DH-PSF image (1.2 μm). If multiple template matches occur too close to one another, the strongest match is chosen, and the others are discarded. A raw fluorescence image of single-molecule PAINT using Nile red is shown in Fig. S5A. DH-PSFs identified by the template matching code are circled in the image.

Once template matching has computed the location of single molecules to integer-pixel precision, these locations are processed by a double Gaussian-fitting algorithm to extract 3D superresolution information. The MATLAB optimization function `lsqnonlin` is used to minimize the mean-square difference between the input data and an eight-parameter double Gaussian model $f(x,y)$ of the DH-PSF, given by

$$f(x,y) = \hat{A}_1 \exp\left\{\frac{-[(x-\hat{x}_1)^2 + (y-\hat{y}_1)^2]}{2\hat{\sigma}_1^2}\right\} + \hat{A}_2 \exp\left\{\frac{-[(x-\hat{x}_2)^2 + (y-\hat{y}_2)^2]}{2\hat{\sigma}_2^2}\right\} + B.$$

Four parameters are used for each Gaussian function: amplitude (\hat{A}_1 and \hat{A}_2), x -center location (\hat{x}_1 and \hat{x}_2), y -center location (\hat{y}_1 and \hat{y}_2), and width ($\hat{\sigma}_1$ and $\hat{\sigma}_2$). The constant offset B is computed from the mean fluorescence background hand-designated in each image. Although this double Gaussian model is only an approximation of the true shape of the DH-PSF (2, 3), it represents a good compromise between fitting accuracy and computational complexity. These fits are then filtered to ensure that they match the data sufficiently accurately and produce good reconstructions of the DH-PSF [i.e., positive amplitudes for both \hat{A}_1 and \hat{A}_2 , an \hat{A}_1/\hat{A}_2 ratio near unity, values of $\hat{\sigma}_1$ and $\hat{\sigma}_2$ between 60 and 180 nm (characteristic sizes of the DH-PSF), etc.].

For the raw fluorescence image shown in Fig. S5A, a reconstruction of all successfully fitted DH-PSFs is shown in Fig. S5B. Eight of the nine DH-PSFs identified by the template matching code were successfully fitted to double Gaussians, validating the code's ability to recognize and fit images of the DH-PSF. This algorithm facilitates the processing of hundreds of thousands of localizations in an efficient and timely manner.

The midpoint between the two fitted Gaussians yields the x and y location of the localized single molecule, whereas the angle between the two Gaussians can be converted into a z position using a calibration curve (see Fig. 1C). Because of aberrations in the $4f$ imaging system, the DH-PSF also slightly translates laterally as a function of the z position of the emitter (3). This effect was removed by measuring the lateral translation of a fluorescent bead as it was scanned along the axial direction (Fig. S6).

Drift Characterization. For superresolution by power-dependent active intermittency and points accumulation for imaging in nanoscale topography (SPRAIPAIN) imaging, the translation of two to three fiducial fluorescent beads were averaged together to track the drift of the microscope stage in time. This measurement is essential for an extended superresolution imaging experiment, as the typical drift of the microscope stage is on the order of hundreds of nanometers. Fig. S7 shows the typical drift measured during a SPRAIPAIN imaging experiment. Overall, the drift

in the y direction is the worst of the three directions but can easily be corrected because of the high precision with which the fiducials are localized (Fig. S7, *Inset*).

Calculation of Localization Precision. The localization precision of each measurement was computed from the previously measured scaling law (2)

$$\sigma_x = \left(\frac{410}{N_{\text{eq}}}\right)^{0.47}, \quad \sigma_y = \left(\frac{550}{N_{\text{eq}}}\right)^{0.52}, \quad \sigma_z = \left(\frac{830}{N_{\text{eq}}}\right)^{0.49},$$

where N is the number of photons detected, B is the measured background per pixel, and $N_{\text{eq}} = 1.5N/\sqrt{B}$ normalizes the difference in background shot noise between our measurements and ref. 2. These equations give a reasonable estimate of the localization precision, because the dominant source of noise in our experiments is photon shot noise.

Calculation of the Cell's Central Axis. The location of each cell's central axis was computed using a custom script written in

1. Brunelli R (2009) *Template Matching Techniques in Computer Vision: Theory and Practice* (Wiley, Chichester, U.K.), p 338.
2. Thompson MA, Lew MD, Badieirostami M, Moerner WE (2010) Localizing and tracking single nanoscale emitters in three dimensions with high spatiotemporal resolution using a double-helix point spread function. *Nano Lett* 10:211–218.

MATLAB. The algorithm works as follows: (i) PAINT localizations from a single cell were rotated in 3D space so that they were aligned with the x axis as closely as possible; (ii) the localizations were partitioned into slices along the x axis (300-nm thick, 100-nm sampling). The thickness and sampling interval for the slices were chosen to ensure that the resulting central axis was smooth. For each slice k , the best center transverse location ($y_{\text{ck}}, z_{\text{ck}}$) was computed by minimizing the standard deviation of the squared distance between the best center location and each localization, given by

$$s_k(y_{\text{ck}}, z_{\text{ck}}) = \sqrt{\frac{1}{N_k - 1} \sum_{i=1}^{N_k} (y_i - y_{\text{ck}})^2 + (z_i - z_{\text{ck}})^2},$$

where y_i, z_i is the transverse position of the i th localization and N_k is the number of localizations in slice k . The aforementioned quantity was minimized by using the MATLAB optimization function `lsqnonlin`. When plotting the cell's central axis, these locations were linearly interpolated.

3. Lew MD, Thompson MA, Badieirostami M, Moerner WE (2010) In vivo three-dimensional superresolution fluorescence tracking using a double-helix point spread function. *Proc SPIE* 7571:75710Z.

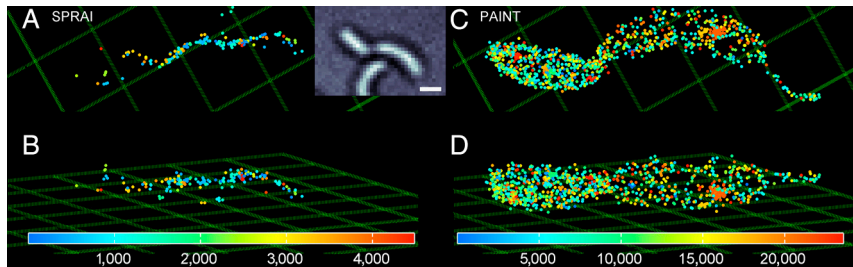


Fig. S1. Localization patterns versus time during SPRAIPAIN data acquisition. (A) The xy projection of localizations on a Crescentin-enhanced YFP (CreS-eYFP) fiber acquired from 4,732 frames of SPRAI imaging. *Inset* shows a transmission white-light image of the same field of view as A. (B) Three-dimensional projection of the fiber shown in A. (C) The xy projection of PAINT localizations of a *Caulobacter crescentus* cell membrane acquired from 23,582 frames of PAINT imaging. (D) Three-dimensional projection of the membrane shown in C. Grid and scale bar, 1 μm . Color bars in units of frames.

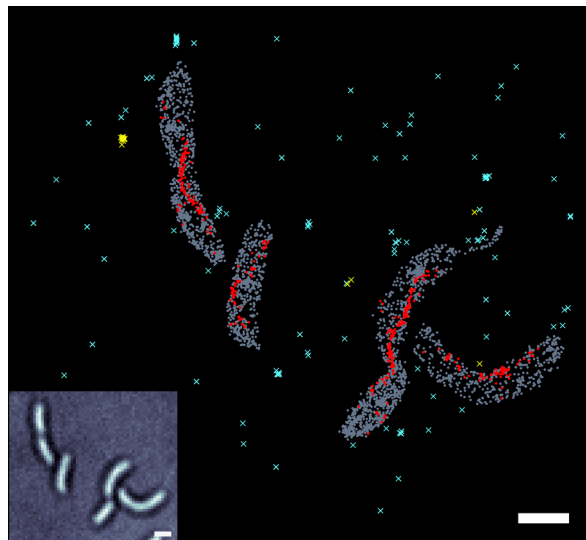


Fig. S2. Analysis of false positive rate of localization for 3D SPRAIPAIN. True SPRAI localizations of Crescentin-enhanced YFP (CreS-eYFP) are shown as red circles; false localizations are shown as yellow \times . True PAINT localizations of the cell membrane are shown as gray circles; false localizations are shown as cyan \times . *Inset* shows a transmission white-light image of the same field of view. Scale bars, 1 μm .

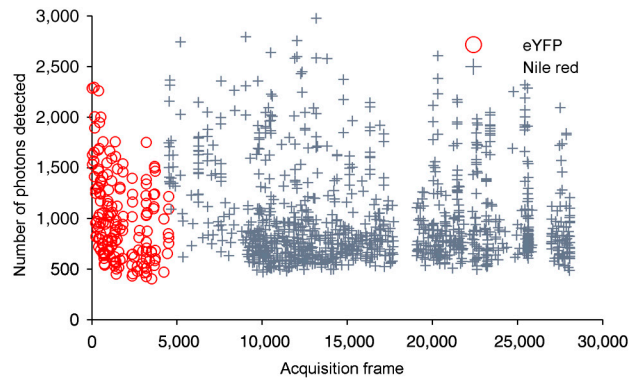


Fig. S3. Number of photons detected per localization versus acquisition time during SPRAIPAIN imaging. Enhanced YFP localizations were acquired during the first 4,499 frames, and the following 23,582 frames were used to collect Nile red localizations. Enhanced YFP localizations are shown as red circles; Nile red localizations are shown as grey crosses.

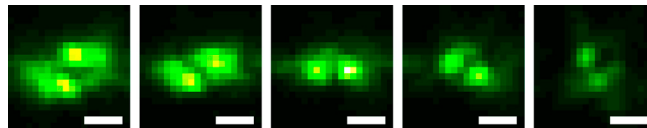


Fig. S4. Templates of the DH-PSF used by the automated template-matching algorithm. These images were taken from a 100-nm fluorescent bead in agarose gel at various z positions. Scale bars, 1 μm .

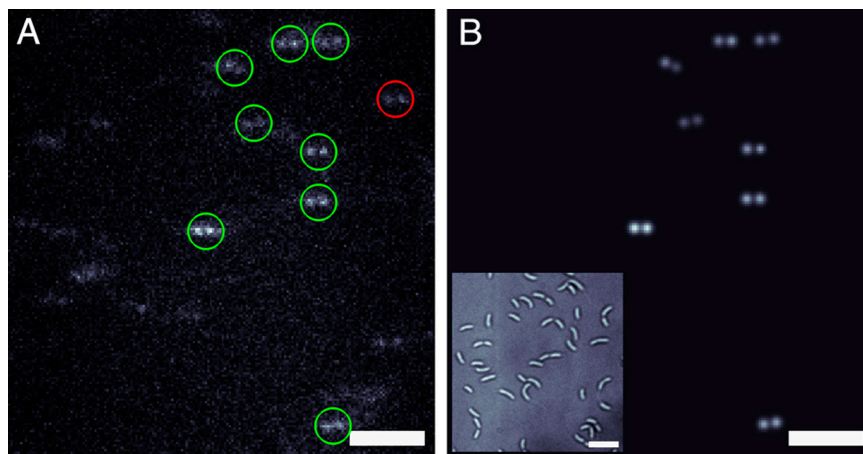


Fig. S5. Validation of the DH-PSF automated recognition and fitting algorithm. (A) Raw fluorescence image of Nile red labeling the cell membranes of *Caulobacter crescentus*. Circles are drawn around DH-PSFs that have been identified by the template-matching algorithm. Successful fits to a double-Gaussian function are shown in green; one unsuccessful fit is in red. (B) Reconstructed image of the successfully fitted DH-PSFs from A. Inset shows a white light transmission image of the same field of view. Scale bars, 5 μm .

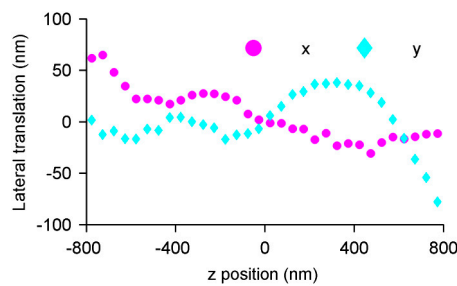


Fig. S6. Lateral translation of the DH-PSF as a function of the z position of an emitter. Translation in the x direction (magenta circles) and y direction (cyan diamonds) is shown over a 1.6- μm depth of field.

